Energy Storage Materials 27 (2020) 591–598

Contents lists available at ScienceDirect

Energy Storage Materials

journal homepage: www.elsevier.com/locate/ensm

Dual anionic vacancies on carbon nanofiber threaded MoSSe arrays: A free-standing anode for high-performance potassium-ion storage

Zhihong Tian [a], Ningbo Chui [a], Ruqian Lian [d], Qifeng Yang [g], Wei Wang [e], Chao Yang [e], Dewei Rao [f], Jiajia Huang [a,*], Yanwu Zhang [a], Feili Lai [b,**], Chuntai Liu [c], Tianxi Liu [b,c]

[a] School of Chemical Engineering and Energy, Zhengzhou University, Zhengzhou, 450001, PR China
[b] Key Laboratory of Synthetic and Biological Colloids, Ministry of Education, School of Chemical and Material Engineering, Jiangnan University, Wuxi, 214122, PR China
[c] Key Laboratory of Materials Processing and Mold (Zhengzhou University), Ministry of Education, Zhengzhou, 450002, PR China
[d] College of Physics, Jilin University, Changchun, 130012, PR China
[e] Department of Materials Science and Engineering, College of Engineering, Peking University, Beijing, 100871, PR China
[f] School of Materials Science and Engineering, Jiangsu University, Zhenjiang, 212013, PR China
[g] Soochow Institute for Energy and Materials Innovations (SIEMIS), Soochow University, Suzhou, 215006, PR China

ARTICLE INFO

Keywords:
Potassium-ion batteries
Dual anionic vacancies
MoSSe
Carbon nanofiber membrane
Density functional theory

ABSTRACT

In spite of the low-cost and abundant potassium resources, the potential commercialization of potassium-ion batteries (PIBs) is still confined by the large-sized K^+ ions and sluggish kinetic process. A flexible free-standing advanced anode for PIBs is synthesized by tactfully incorporating dual anionic vacancies on MoSSe arrays in combination of carbon nanofiber membrane (v-MoSSe@CM). The vacancy-rich MoSSe arrays in v-MoSSe@CM dramatically enhance the adsorption of K^+ ions, leading to a higher capacity of 370.6 mAh g^{-1} at 0.1 A g^{-1} over 60 cycles as compared with that 168.5 mAh g^{-1} of vacancy-free MoSSe@CM. Meanwhile, the density functional theory (DFT) calculations demonstrate a facilitated ability for K^+ insertion into v-MoSSe interlayers with a much more negative adsorption value of −1.74 eV than that (0.53 eV) of vacancy-free MoSSe. The thousands of carbon nanofiber-supported three-dimensional frameworks can not only inhibit the agglomeration of MoSSe nanosheets, but also remit the volume expansion and avoid possible collapse of the nanostructures during cycling, resulting into a high capacity retention of 220.5 mAh g^{-1} at 0.5 A g^{-1} after 1000 cycles. Therefore, this work uncovers the relationship between vacancy engineering and potassium-ion storage performance, guiding a feasible route to develop potential materials for potassium-ion battery.

1. Main texts

The increasing demands for sustainable and green energy storage systems have triggered the extensive researches on lithium-ion batteries (LIBs) over past decades, which are regarded as the most promising devices for consumer electronics and electric vehicles due to their high energy density and power density [1,2]. However, the severely limited lithium resources have already become one of the greatest challenges in the further development of LIBs, making other earth-abundant alkali-metal elements (*e.g.* sodium [3] and potassium [4–9]) potential candidates for next generation batteries. As compared to the redox of Na/Na^+ (−2.71 V), the K/K^+ shows a more negative potential of −2.93 V *vs.* standard hydrogen electrode [10–12], which makes potassium-ion batteries (PIBs) promising prospect in large-scale stationary applications. However, the researches on PIBs are still in early infancy, and subjected to the large radius of K^+ ion. Therefore, the key point to achieve high-performance PIBs becomes on how to design artful anode materials with suitable interlayer spacing for feasible intercalation/deintercalation of K^+ ion [13–16].

Transition metal dichalcogenides (TMDs) belong to an important family of alkali-ion intercalation materials, which have been widely used as anodes in LIBs [17], sodium-ion batteries (NIBs) [18] and PIBs [15,19], due to their lamellar crystal structure for efficient alkali-ion intercalation/deintercalation. However, a well grown TMD crystal would always confine the intercalation/deintercalation process in a parallel direction as the crystal face. Therefore, a defect-rich structure may create

* Corresponding author.
** Corresponding author.
E-mail addresses: huangjiajia@zzu.edu.cn (J. Huang), fllai14@fudan.edu.cn (F. Lai).

https://doi.org/10.1016/j.ensm.2019.12.016
Received 8 August 2019; Received in revised form 2 December 2019; Accepted 7 December 2019
Available online 11 December 2019

new channels in perpendicular directions for faster transfer of alkali-ions into the interlayer space. As a typical kind of point defects [20–22], vacancy engineering has already been discovered its positive effect in some energy storage systems (*e.g.* nitrogen-doped carbon nanofiber@MoS_2 nanosheets arrays with S-vacancies [23] and nanosheet assembled hollow single-hole Ni–Co–Mn oxide spheres [24]) as the incorporated vacancies can not only provide new ion channels but also act as activated regions for ion adsorption. To our knowledge, the function of anionic vacancy is still veiled in the area of potassium-ion battery, making it necessary to conduct investigations to reveal the possible relationship between vacancy engineering and potassium-ion storage behavior. In another perspective, the drawbacks of TMDs are still obvious even after vacancy incorporation (such as poor electrical conductivity and huge volume expansion), which result into the poor rate performance and short cycling lifespan of PIBs. Up to now, it has been regarded as an effective method to solve the above issues by constructing TMDs-based hybrid nanostructures with carbonaceous matrices [25–27]. However, the majority of carbonaceous matrices are confined by the cumbersome process for electrode preparation by blending conductive and binding agents. The introduction of excess binding agents may severely affect the release of electrochemical properties of electroactive TMDs. Thus, superior binder-free and free-standing carbon matrices are urgently needed for the development of PIBs. Electrospinning is a promising and straightforward technique that produces free-standing nanofiber membranes with unique three-dimensional (3D) fiber network, good structural stability, high flexibility and easily controllable thickness [28,29]. The carbonized nanofiber membrane (CM) is used as a good carbon substrate material, which can improve the electronic conductivity and efficiently avoid the tedious preparation process of electrodes by using binders and conductive additives. In addition, the 3D network of CM can also increase the number of electroactive sites by achieving the uniform dispersion of TMD nanoparticles.

Herein, a flexible free-standing anode was designed by anchoring dual anionic vacancy-rich MoSSe arrays on an electrospun carbon nanofibers membrane for high-performance potassium-ion battery. The as-prepared dual anionic vacancy-rich MoSSe arrays in combination of carbon nanofibers membrane (v-MoSSe@CM) deliver a higher capacity of 370.6 mAh g^{-1} at a current density of 0.1 A g^{-1} after 60 cycles than that (168.5 mAh g^{-1}) of vacancy-free MoSSe@CM, which is due to the much more negative adsorption energy of −1.74 eV for K^+ ions after the introduction of dual anionic vacancies. In addition, the porous interfibrous space in CM is beneficial to accommodating the volume expansion and avoiding possible collapse of the nanostructures during cycling. As a result, the v-MoSSe@CM composite exhibits good rate performance at a series of current densities, and shows a high discharge capacity (220.5 mAh g^{-1}) at a high current density of 0.5 A g^{-1} after 1000 cycles, demonstrating the promising application of v-MoSSe@CM in high-performance PIBs.

The dual anionic vacancy-rich MoSSe arrays in combination of carbon nanofiber membrane (v-MoSSe@CM) were prepared by using electrospun carbon nanofibers (CM) as a flexible substrate after undergoing hydrothermal, washing, and annealing processes (Fig. 1a). Firstly, CM substrate was produced by pre-oxidizing and carbonizing electrospun polyacrylonitrile nanofibers membrane under an inert atmosphere. As the scanning electron microscopy (SEM) image shown in Fig. 1b and S1, the carbon nanofibers possess smooth surface and uniform diameter at ~370 nm. The well-connected three-dimensional carbon nanofibers provide an excellent framework for further anchoring of v-MoSSe arrays, making the hybrid as an integrity.

The final product of v-MoSSe@CM was displayed in Fig. S2, which still maintains high flexibility and integrity after the hydrothermal reaction. As revealed in Fig. 1c, MoSSe arrays are uniformly anchored on the surface of carbon nanofibers, which are consisted of thousands of ultrathin MoSSe nanosheets. The homogeneous anchoring of MoSSe

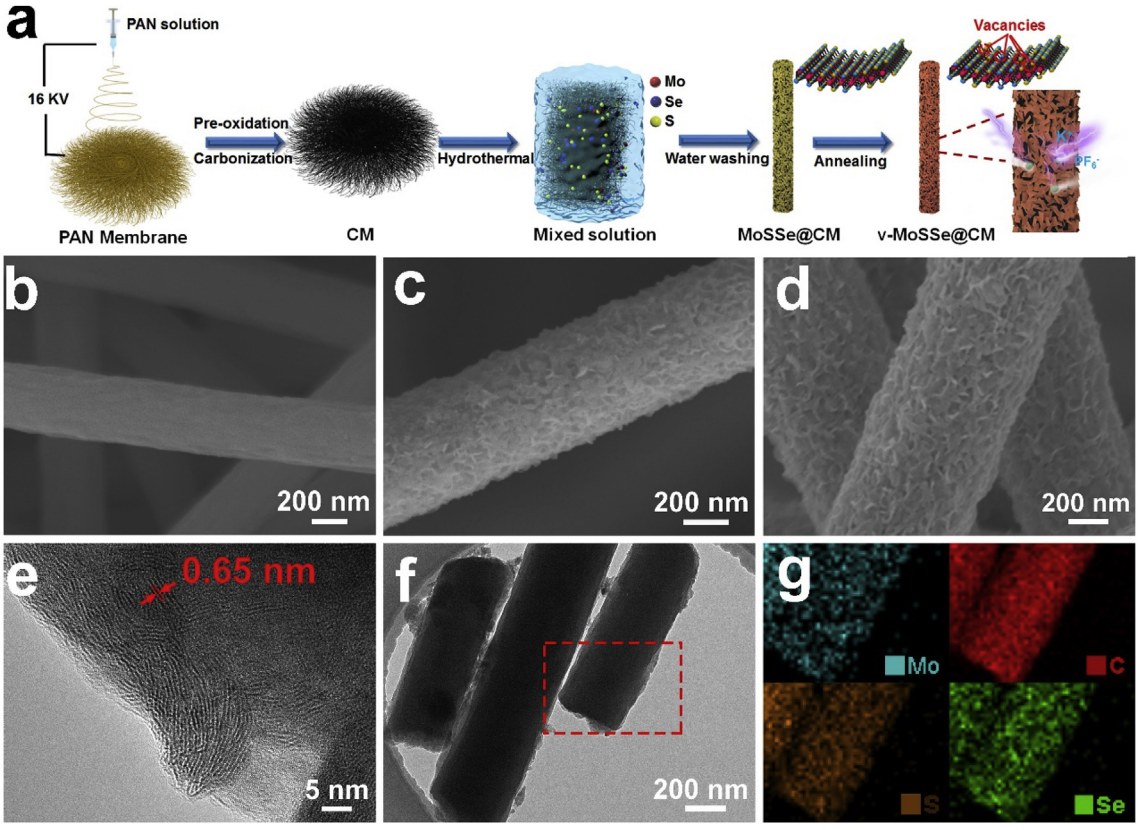

Fig. 1. a) Schematic illustration of the preparation of v-MoSSe@CM. SEM images of b) CM, c) MoSSe@CM, and d) v-MoSSe@CM. e, f) HRTEM and TEM images of the v-MoSSe@CM. g) Elemental mapping images of the v-MoSSe@CM.

arrays prevents the severe aggregation of bulk MoSSe powder. As a result, more exposed MoSSe surface can be obtained with increased effective specific surface area of the MoSSe component. Meanwhile, the v-MoSSe@CM displays an unchanged morphology after incorporating dual anionic vacancies (Fig. 1d), which indicates that annealing process only occurs within an atomic level. The loading content of v-MoSSe arrays in v-MoSSe@CM is also calculated to be about 54.7% from the TGA curves (Fig. S3). The high resolution TEM image of v-MoSSe@CM (Fig. 1e) displays a typical interlayer spacing of ~0.65 nm, which is between the values of MoS_2 and $MoSe_2$ (Figs. S4 and S5). The different radius and electronegativity between S and Se atoms are beneficial for the generation of crystal distortion after hydrothermal reaction process, resulting MoSSe into a metastable status, which provides favorable conditions for the successful and possible introduction of anionic vacancies [30,31]. In addition, the TEM image of the v-MoSSe@CM (Fig. 1f) proves the successful anchoring of abundant v-MoSSe layers with a close connection on the surface of carbon nanofibers. Meanwhile, the TEM image of MoSSe@CM is displayed in Fig. S6, which also provides a compelling evidence to prove the unchanged micro-structure of v-MoSSe@CM after the annealing process. Furthermore, the energy-dispersive X-ray spectroscopy mapping images (Fig. 1g) demonstrate the homogeneous spatial distribution of Mo, Se, and S elements into the hybrid nanofibers.

As shown in the X-ray diffraction (XRD) patterns (Fig. 2a), all of the MoS_2, MoSSe and $MoSe_2$ display two broad diffraction patterns at $2\theta \approx 32^\circ$ and 55°, which correspond to (100) and (110) planes. Since the radius of S atom is smaller than that of Se atom, the positions of diffraction patterns for the MoSSe are located between those of the MoS_2 and $MoSe_2$, which fairly agreed with the VegardQs law [30,32]. Fig. 2b shows the XRD patterns of CM, v-MoSSe@CM, MoSSe@CM, and MoSSe. The peaks at $2\theta \approx 24^\circ$, 32° and 55° indicate the coexistence of MoSSe and CM compounds in both of v-MoSSe@CM and MoSSe@CM. Meanwhile, their similar XRD patterns demonstrate that the annealing process has no significant effect on the crystal structure of MoSSe. Furtherly, X-ray photoelectron spectra (XPS) measurements were also carried out to analyze the chemical composition and state of v-MoSSe@CM and MoSSe@CM. In the survey spectra of v-MoSSe@CM (Fig. S7), characteristic peaks for C, Mo, Se, and S appear as the principal elements, which demonstrate the successful generation of the hybrid without detectable impurities. It is shown that two characteristic peaks located at 229.1 and 232.2 eV are observed from Mo $3d_{5/2}$ and Mo $3d_{3/2}$ orbitals, suggesting the dominance of Mo (IV) in the product (Fig. S8) [33,34]. For the high-resolution spectra of Se 3p, S 2p and Se 3d shown in Fig. 2c and d, all of these peaks slightly shift to lower binding energies with values between 0.2 and 0.6 eV after the annealing process, when compared with those peaks in vacancy-free MoSSe@CM, indicating the successful incorporation of sulfur and selenium vacancies in the v-MoSSe@CM composite [22,35]. As the electron paramagnetic resonance (EPR) results shown in Fig. S9, the v-MoSSe@CM composite displays two big symmetrical peaks in $g = 2.002$, while the MoSSe@CM composite shows a straight line without any obvious peaks. It provides another convincing evidence for the anionic vacancies in the v-MoSSe@CM composite [36], agreeing well with the above XPS results.

In addition, there are thousands of possibilities for the potential distribution of dual anionic vacancies in v-MoSSe@CM. In order to simplify the problem, three bivacant v-MoSSe models with different vacancy distributions are constructed as bivacant model 1-3 based on the intact MoSSe model (Fig. 2e). Under the guidance of density functional theory (DFT) calculation, both of bivacant model 2 and 3 display higher relative energy values of 0.0085 and 0.0239 eV, respectively, as compared with the reference substance of bivacant model 1. These results indicate the S and Se vacancies tend to be generated as adjacent anionic vacancy pairs (bivacant model 1).

In order to demonstrate the function of dual anionic vacancy, v-MoSSe@CM and other contrast samples are used as anodes in PIBs. In the discharging process, the v-MoSSe@CM accepts the electron and creates reduction reaction, charging is the opposite (Fig. S10). Fig. 3a shows the cyclic voltammogram (CV) curves of v-MoSSe@CM at a scan rate of 0.1 mV s^{-1} between 0.01 and 3.0 V. In the first cycle, there are three reduction peaks in the cathodic scan, and their peaks are located at 0.23, 0.68 and 0.82 V. However, these three reduction peaks disappeared in subsequent scans, which are due to the formation of solid electrolyte interphase (SEI) and slight change in the structure of electrodes to accommodate the insertion of K^+ ions. Two peaks appear at 0.73 V and 1.86 V in the anodic processes, indicating that K^+ is extracted from the anode. In the second scan, two new cathodic peaks appear at 0.99 and 1.29 V, which are related to two stages of the reactions from MoSSe to K_2S and K_2Se. The reduction peak at 1.29 V can be assigned to the insertion of K^+ into the interlayers of MoSSe to form K_xMoSSe. The second reduction peak at 0.99 V is associated with the conversion of K_xMoSSe to K_2Se and K_2S. Another anodic peak at 1.86 V corresponds to the reaction from K_2Se and K_2S to MoSSe [19,37]. The anodic and cathodic peaks are similar in the following scans.

To demonstrate the working mechanism of the electrodes, ex-situ XRD was performed to characterize the electrode at different states during the 10th discharge/charge process (Fig. 3b). The peaks of the full charged (F–C) merge at $2\theta = 31.7^\circ$, 37.8°, 47.1°, corresponding to MoSSe. In addition, other peaks at $2\theta = 30.2^\circ$, 39.2°, 49.3° and 54.5° could be attributed to the crystals of $Mo_{15}Se_{19}$ and $Mo_{15}S_{19}$ that produced after the formation of SEI [38]. When discharged to 1.5 V (D-1.5 V) and charged to 1.8 V (C-1.8 V), the new appeared peaks at $2\theta = 32.6^\circ$, 37.8°, 57.6° could be regarded as the K_xMoSSe. Furtherly, these peaks are weakened or diminished when discharged to 1.0V (D-1.0 V) and charged to 2.0 V (C-2.0 V). After fully discharged (F-D), the characteristic MoSSe peaks diminish with another three appeared peaks at $2\theta = 34.2^\circ$, 50.5° and 38.4° corresponding to (220) and (420) of K_2S, and (311) of K_2Se, respectively, which indicates the formation of the potassium compound *via* the conversion reaction at the end of the discharging process [39,40]. Based on the above discussion, the electrochemical reactions of the discharge/charge could be described as the following steps:

$$MoSSe + xK^+ + xe^- \rightarrow K_xMoSSe$$

$$K_xMoSSe + (4-x)K^+ + (4-x)e^- \rightarrow K_2S + K_2Se + Mo$$

The charge/discharge profiles of the v-MoSSe@CM at a current density of 0.5 A g^{-1} are shown in Fig. 3c. The discharge capacities are 295.6 and 245.6 mAh g^{-1} for the second and tenth cycles, respectively, and the capacity loss is attributed to some irreversible processes (such as the formation of the SEI layer). The discharge capacity for the two-hundredth cycle is 234.2 mAh g^{-1} with a high Coulombic efficiency of about 100%. The slow fading capacity from tenth to two-hundredth cycles indicates the outstanding reversibility and stability of v-MoSSe@CM anode.

To compare the rate performance of the v-MoSSe@CM, MoSSe@CM, and MoSSe for PIBs, their specific capacities are recorded under different current densities from 0.1 to 5.0 A g^{-1} (Fig. 3d). The reversible capacities for v-MoSSe@CM are calculated to be 389.6, 348.7, 315.6, 276.8, 250.8, and 202.6 mAh g^{-1} under different charge/discharge current densities of 0.1, 0.2, 0.5, 1.0, 2.0, and 5.0 A g^{-1}, respectively, which shows an excellent performance compared to previously reported electrodes for PIBs (Table S1). After 5 cycles under a current density of 0.1 A g^{-1}, v-MoSSe@CM, bulk MoSSe, and MoSSe@CM anodes display capacities of 389.6, 99.8, and 193.7 mAh g^{-1}, respectively. After operating over 60 cycles under different current densities, a high capacity of 370.6 mAh g^{-1} can still be maintained at a current density of 0.1 A g^{-1} for v-MoSSe@CM anode, demonstrating its superior rate performance. On the contrary, the vacancy-free MoSSe@CM only shows a much lower capacity of 168.5 mAh g^{-1} at a current density of 0.1 A g^{-1}, which demonstrates the positive role of anionic vacancy in enhancing the energy storage property of PIBs. Long-term cycling stability is regarded as a crucial criterion for the practical application of PIBs, which is also operated for v-MoSSe@CM

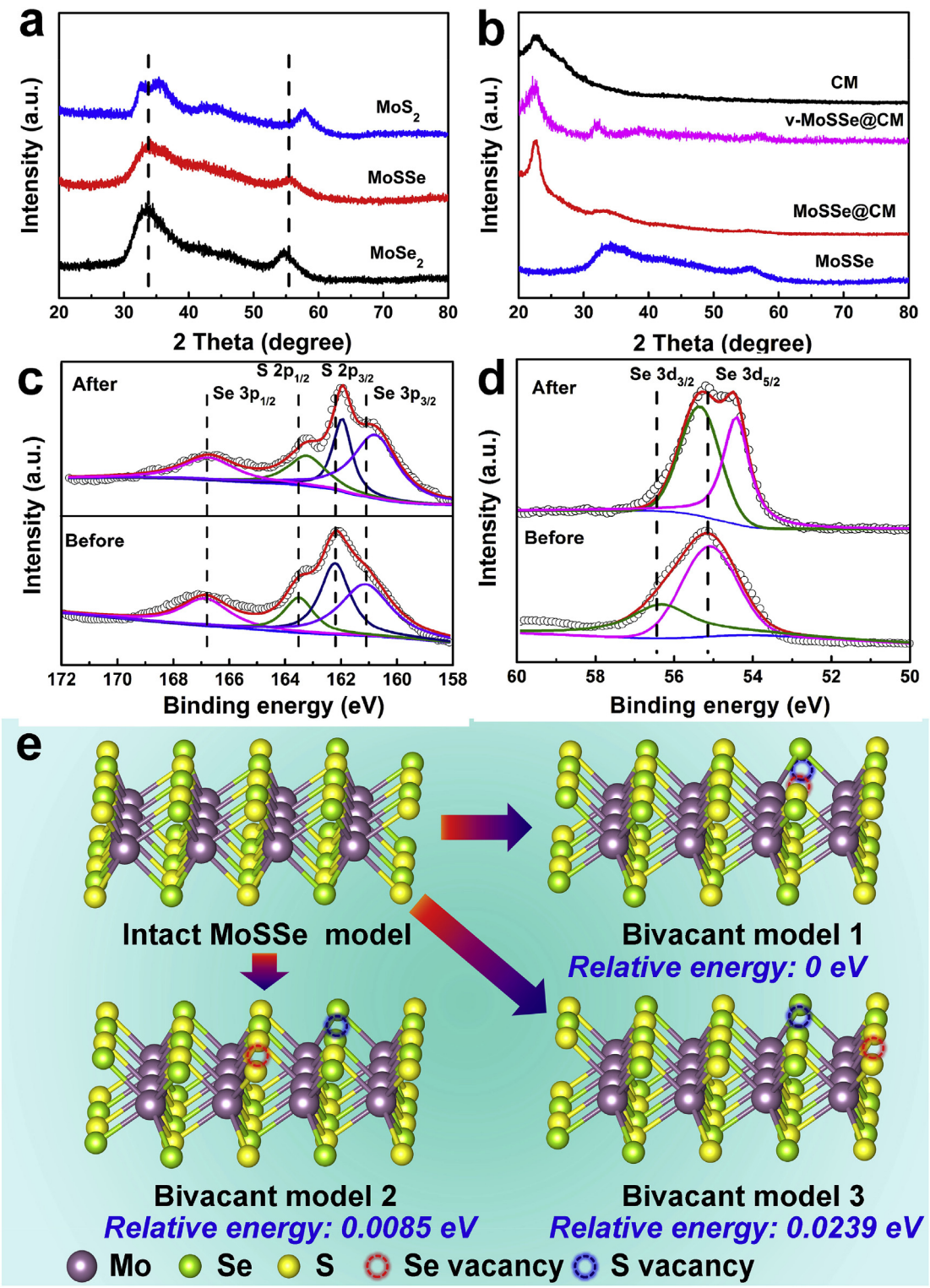

Fig. 2. a) X-ray diffraction patterns of MoS_2, MoSSe and $MoSe_2$. b). X-ray diffraction patterns of CM, v-MoSSe@CM, MoSSe@CM, and MoSSe. c) High-resolution spectra of the S 2p and Se 3p peaks of the MoSSe@CM before and after annealing process. d) High-resolution spectra of the Se 3d peaks of MoSSe@CM before and after annealing process. e) Bivacant models with corresponding relative energies after incorporating three different types of dual anionic vacancies.

anode at a high current density of 0.5 A g^{-1} (Fig. 3e). After 1000 cycles, a high discharge capacity of 220.5 mAh g^{-1} can still be maintained with a capacity retention of 84.6% (Fig. S11). In addition, the excellent cycling stability can also be demonstrated by the well-maintained CV curve for v-MoSSe@CM after long-term cycling test as the one before cycling (Fig. S12).

To gain an in-depth understanding between the incorporated dual anionic vacancies and enhanced PIBs performance, the density functional theory (DFT) calculations are carried out. Firstly, the surface electronic structures are revealed by density of states (DOS). As shown in Fig. 4a and b, the bivacant model 1 shows a much narrower bandgap than that in intact MoSSe model, indicating its better charge transfer ability after

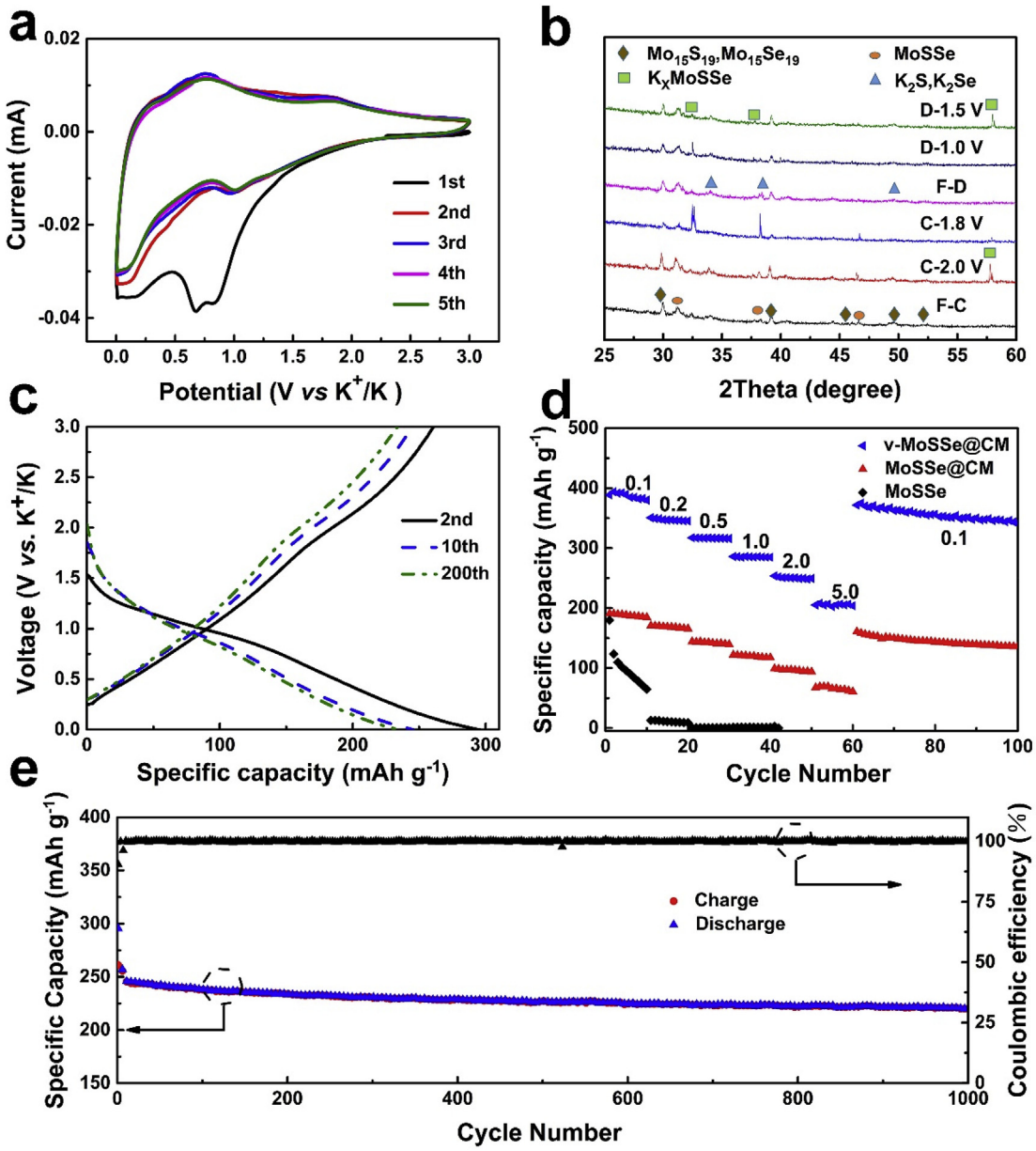

Fig. 3. a) CV curves for the v-MoSSe@CM in the first five cycles at a scan rate of 0.1 mV s^{-1}. b) Ex-situ XRD patterns at different states during the discharge/charge process. c) The 2nd, 10th, and 200th charge/discharge curves of v-MoSSe@CM at 0.5 A g^{-1} for PIBs. d) Rate performance under different current densities of the as-prepared v-MoSSe@CM, MoSSe@CM, and MoSSe. The unit for the current density is A g^{-1}. e) Long-term cycling stability and Coulombic efficiency at a high current density of 0.5 A g^{-1} over 1000 cycles.

incorporating dual anionic vacancies. As the partial charge density shown in Fig. 4c, the dual anionic vacancies in bivacant model 1 are beneficial for the charge transfer from the inserted K^+ ion to the v-MoSSe surface, leading to a better connection between the v-MoSSe@CM anode and KPF_6 electrolyte. In addition, the v-MoSSe shows a much more negative energy for the insertion of K^+ (−1.74 eV) than that (0.53 eV) of the intact MoSSe model, which demonstrates the initial anode-K^+ state can be easily achieved in the interlayer space of v-MoSSe arrays for v-MoSSe@CM anode. As a result, the theoretical results prove that the v-MoSSe can provide more efficient active sites for the store of K^+ ions, showing their considerable consistency with the experimental observations (the enhanced PIBs property of v-MoSSe@CM anode).

Furtherly, the kinetic analysis for v-MoSSe@CM was conducted by investigating its capacitive behavior. The CVs were carried out at stepped scan rates (0.2–5 mV s^{-1}) in a voltage range from 0.01 to 3.0 V (Fig. 5a). The adjustable constant of b can be extracted from the slope by plotting $\log(i)$ against $\log(v)$ as the following equations:

$$i = av^b \tag{1}$$

$$\log i = \log a + b \log v \tag{2}$$

Where i is peak current, v is scan rate, a and b are adjustable constants. Based on the value of b, the current can be controlled by two possible processes as semi-infinite linear diffusion ($b = 0.5$) and surface-controlled diffusion ($b = 1$) [41,42]. As displayed in Fig. 5b, both the anodic and cathodic processes for v-MoSSe@CM show good linear relationship with adjustable constant b values of 0.99 and 0.97, respectively, suggesting that a fast kinetics is dominated by a surface process for v-MoSSe@CM.

To further study the capacitive behavior, the capacitive contribution ratio under different scan rates can be quantified through the following

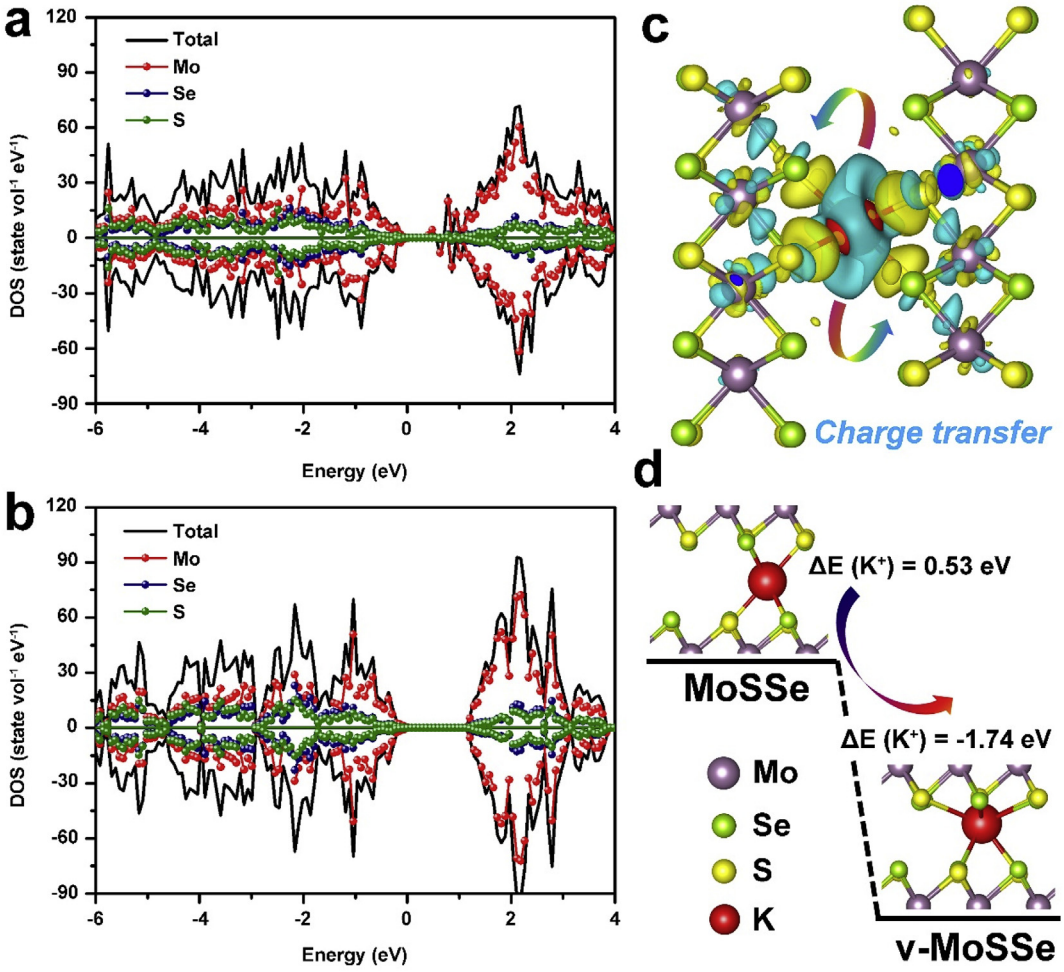

Fig. 4. Calculated density of states for a) bivacant model 1, and b) intact MoSSe model. c) Partial charge density of bivacant model 1 after inserting K^+. d) Calculated energy for the insertion of K^+ in intact MoSSe model and bivacant model 1 (v-MoSSe).

equations:

$$I(V) = k_1 v + k_2 v^{1/2} \tag{3}$$

$$I(V) \,/\, v^{1/2} = k_1 v^{1/2} + k_2 \tag{4}$$

where $k_1 v$ and $k_2 v^{1/2}$ represent the contribution of capacitance and ionic diffusion, respectively [43,44]. After dividing $v^{1/2}$ on both sides of Equation (3), Equation (4) can be obtained successfully. When charging at scan rate of 0.2 mV s^{-1}, the capacitive contribution value is below 0.5 (Fig. S14), indicating that the charge storage behavior in v-MoSSe@CM is dominated by the ionic diffusion process at a low scan rate. Fig. 5c shows the CV profile with the capacitive contribution at scan rate of 1 mV s^{-1}, from which the capacitive contribution value is fixed to be 0.576. With increasing the scan rates, the capacitive charge contribution becomes higher and finally reaches to a maximum value of 0.792 at a high scan rate of 5 mV s^{-1} (Fig. 5d and S15), meaning that capacitive behavior would play a leading role towards capacity contribution at high scan rate.

In summary, a flexible advanced PIBs anode of v-MoSSe@CM was synthesized by combining hydrothermal reaction and annealing process. The introduced dual anionic vacancy-rich v-MoSSe arrays can effectively improve its electrochemical performance by dramatically enhancing the adsorption ability of K^+ ions and accelerating the electron transfer during electrochemical process. Therefore, v-MoSSe@CM displays a higher capacity of 370.6 mAh g^{-1} at 0.1 A g^{-1} over 60 cycles as compared with that (168.5 mAh g^{-1}) of vacancy-free MoSSe@CM, which proves the positive role of anionic vacancy in the field of high-performance electrodes for PIBs. Furthermore, the DFT calculations also demonstrate a facilitated ability for K^+ insertion into v-MoSSe interlayers with a much more negative adsorption value of −1.74 eV than that (0.53 eV) of vacancy-free MoSSe. Meanwhile, the unique 3D networks of CM could buffer the volume expansion and stabilize the integral structure. As a result, the v-MoSSe@CM anode could still retain 220.5 mAh g^{-1} after 1000 cycles at a high current density of 0.5 A g^{-1}, with a capacity fading of only 0.015% per cycle, demonstrating its potential applications in high-performance PIBs.

Author contributions

Z. H. Tian: Writing – original draft, conceived the idea, conducted the synthesis and characterizations. N. B. Chui: Writing - original draft, conceived the idea, conducted the synthesis and characterizations. T. X. Liu: conceived the idea and cowrote the paper. F. L. Lai: Writing – original draft and conceived the idea. J. J. Huang: supervised the project. Y. W. Zhang: supervised the project. C. T. Liu: supervised the project. Q. F. Yang: conducted the synthesis and characterizations. W. Wang: tested the battery performance. C. Yang: tested the battery performance. R. Q. Lian: conducted theoretical calculations. D. W. Rao: conducted theoretical calculations. All the authors discussed the results and commented on the manuscript.

Data availability

The raw/processes data required to reproduce these findings cannot

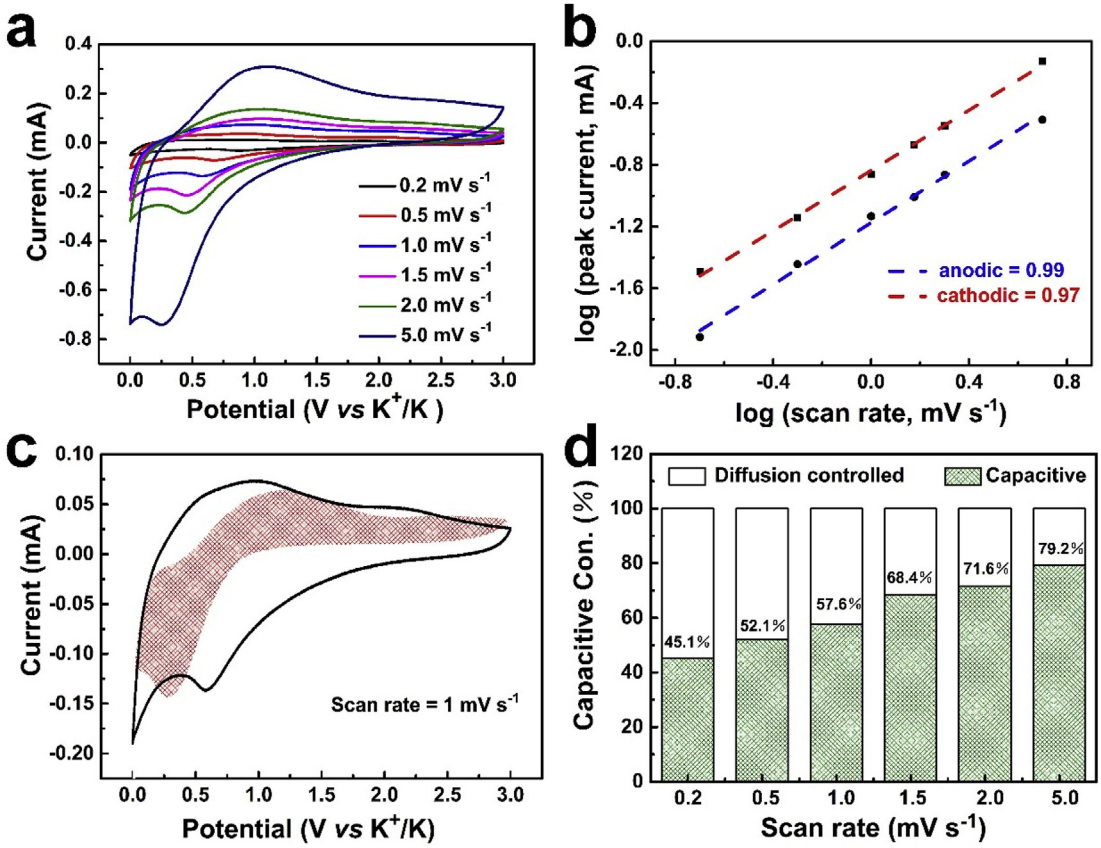

Fig. 5. a) CV profiles at different scan rates. b) The plots of log (i) vs. log(υ) (peak current: i, scan rate: υ) of v-MoSSe@CM. c) The red region shows the CV profile with the capacitive charge storage contributions at scan rate of 1 mV s^{-1}. d) The corresponding percentage of capacitive charge storage contributions at different scan rates.

be shared at this time due to technical or time limitations. Data will be made available by the corresponding author upon request.

Declaration of competing interest

The authors declare that they have no known competing financial interests or personal relationships that could have appeared to influence the work reported in this paper.

Acknowledgements

This work was supported by the National Natural Science Foundation of China (No. 51873198 and 51503184).

Appendix A. Supplementary data

Supplementary data to this article can be found online at https://doi.org/10.1016/j.ensm.2019.12.016.

References

[1] B. Dunn, H. Kamath, J. Tarascon, Electrical energy storage for the grid: a battery of choices, Science 334 (2011) 928–935.
[2] Y. Zou, S. Chen, X. Yang, N. Ma, Y. Xia, D. Yang, S. Guo, Suppressing Fe–Li antisite defects in $LiFePO_4$/carbon hybrid microtube to enhance the lithium ion storage, Adv. Energy Mater. 6 (2016), 1601549.
[3] C. Wang, L. Wang, F. Li, F. Cheng, J. Chen, Bulk bismuth as a high-capacity and ultralong cycle-life anode for sodium-ion batteries by coupling with glyme-based electrolytes, Adv. Mater. 29 (2017), 1702212.
[4] Y. Xu, S. Duan, Y. Sun, D. Bin, X. Tao, D. Zhang, Y. Liu, A. Cao, L. Wan, Recent developments in electrode materials for potassium-ion batteries, J. Mater. Chem. A 7 (2019) 4334–4352.
[5] K. Kubota, M. Dahbi, T. Hosaka, S. Kumakura, S. Komaba, Towards K-ion and Na-ion batteries as "beyond Li-ion", Chem. Rec. 18 (2018) 459–479.
[6] J. Ding, H. Zhang, H. Zhou, J. Feng, X. Zheng, C. Zhong, E. Paek, W. Hu, D. Mitlin, Sulfur-grafted hollow carbon spheres for potassium-ion battery anodes, Adv. Mater. 31 (2019), 1900429.
[7] C. Yang, F. Lv, Y. Zhang, J. Wen, K. Dong, H. Su, F. Lai, G. Qian, W. Wang, A. Hilger, Y. Xu, Y. Zhu, Y. Deng, W. Hu, I. Manke, Y. Chen, Confined Fe_2VO_4⊂nitrogen-doped carbon nanowires with internal void space for high-rate and ultrastable potassium-ion storage, Adv. Energy Mater. 9 (2019) 1902674.
[8] K. Han, Z. Liu, P. Li, Q. Yu, W. Wang, C. Lao, D. He, W. Zhao, G. Suo, H. Guo, L. Song, M. Qin, X. Qu, High-throughput fabrication of 3D N-doped graphenic framework coupled with Fe_3C@porous graphite carbon for ultrastable potassium ion storage, Energy Storage Mater. 22 (2019) 185–193.
[9] X. Niu, Y. Zhang, L. Tan, Z. Yang, J. Yang, T. Liu, L. Zeng, Y. Zhu, L. Guo, Amorphous $FeVO_4$ as a promising anode material for potassium-ion batteries, Energy Storage Mater. 22 (2019) 160–167.
[10] W. Zhang, Y. Liu, Z. Guo, Approaching high-performance potassium-ion batteries via advanced design strategies and engineering, Sci. Adv. 5 (2019) eaav7412.
[11] C. Chen, Y. Yang, X. Tang, R. Qiu, S. Wang, G. Cao, M. Zhang, Graphene-encapsulated FeS_2 in carbon fibers as high reversible anodes for Na^+/K^+ batteries in a wide temperature range, Small 15 (2019), 1804740.
[12] J. Ruan, Y. Zhao, S. Luo, T. Yuan, J. Yang, D. Sun, S. Zheng, Fast and stable potassium-ion storage achieved by in situ molecular self-assembling N/O dual-doped carbon network, Energy Storage Mater. 23 (2019) 46–54.
[13] L. Fan, K. Lin, J. Wang, R. Ma, B. Lu, A nonaqueous potassium-based battery–supercapacitor hybrid device, Adv. Mater. 30 (2018), 1800804.
[14] B. Kishore, G. Venkatesh, N. Munichandraiah, $K_2Ti_4O_9$: a promising anode material for potassium ion batteries, J. Electrochem. Soc. 163 (2016) A2551–A2554.
[15] W. Wang, B. Jiang, C. Qian, F. Lv, J. Feng, J. Zhou, K. Wang, C. Yang, Y. Yang, S. Guo, Pistachio-shuck-like $MoSe_2$/C core/shell nanostructures for high-performance potassium-ion storage, Adv. Mater. 30 (2018), 1800804.
[16] C. Zeng, F. Xie, X. Yang, M. Jaroniec, L. Zhang, S. Qiao, Confined transformation derived ultrathin titanate nanosheets/graphene films for excellent Na/K ion storage, Angew. Chem. Int. Ed. 57 (2018) 8540–8544.
[17] I. Sahroni Riyanto, K. Bindumadhavan, P. Chang, R. Doong, Boron doped graphene quantum structure and MoS_2 nanohybrid as anode materials for highly reversible lithium storage, Front. Chem. 7 (2019) 116.
[18] Z. Hu, L. Wang, K. Zhang, J. Wang, F. Cheng, Z. Tao, J. Chen, MoS_2 nanoflowers with expanded interlayers as high-performance anodes for sodium-ion batteries, Angew. Chem. Int. Ed. 53 (2014) 12794–12798.
[19] X. Ren, Q. Zhao, W. McCulloch, Y. Wu, MoS_2 as a long-life host material for potassium ion intercalation, Nano Res. 10 (2017) 1313–1321.

[20] D. Sim, M. Kim, S. Yim, M. Choi, J. Choi, S. Yoo, Y. Jung, Controlled doping of vacancy-containing few-layer MoS_2 via highly stable thiol-based molecular chemisorption, ACS Nano 9 (2015) 12115–12123.
[21] W. Zong, F. Lai, G. He, J. Feng, W. Wang, R. Lian, Y. Miao, G. Wang, I. Parkin, T. Liu, Sulfur-deficient bismuth sulfide/nitrogen-doped carbon nanofibers as advanced free-standing electrode for asymmetric supercapacitors, Small 14 (2018) 1801562.
[22] D. Gao, B. Xia, Y. Wang, W. Xiao, P. Xi, D. Xue, J. Ding, Dual-native vacancy activated basal plane and conductivity of $MoSe_2$ with high-efficiency hydrogen evolution reaction, Small 14 (2018) 1704150.
[23] J. Liang, Z. Wei, C. Wang, J. Ma, Vacancy-induced sodium-ion storage in N-doped carbon Nanofiber@MoS_2 nanosheet arrays, Electrochim. Acta 285 (2018) 301–308.
[24] S. Li, X. Zhao, Y. Feng, L. Yang, X. Shi, P. Xu, J. Zhang, P. Wang, M. Wang, R. Che, A flexible film toward high-performance lithium storage: designing nanosheet-assembled hollow single-hole Ni–Co–Mn–O spheres with oxygen vacancy embedded in 3D carbon nanotube/graphene network, Small 15 (2019), 1901343.
[25] H. Huang, J. Cui, G. Liu, R. Bi, L. Zhang, Carbon-coated $MoSe_2$/MXene hybrid nanosheets for superior potassium storage, ACS Nano 13 (2019) 3448–3456.
[26] B. Jia, Q. Yu, Y. Zhao, M. Qin, W. Wang, Z. Liu, C. Lao, Y. Liu, H. Wu, Z. Zhang, X. Qu, Bamboo-like hollow tubes with MoS_2/N-doped-C interfaces boost potassium-ion storage, Adv. Funct. Mater. 28 (2018), 1803409.
[27] H. Hong, J. Liu, H. Huang, C. Etogo, X. Yang, B. Guan, L. Zhang, Ordered macro-microporous metal-organic framework single crystals and their derivatives for rechargeable aluminum-ion batteries, J. Am. Chem. Soc. 141 (2019) 14764–14771.
[28] Y. Miao, Y. Huang, L. Zhang, W. Fan, F. Lai, T. Liu, Electrospun porous carbon nanofiber@MoS_2 core/sheath fiber membranes as highly flexible and binder-free anodes for lithium-ion batteries, Nanoscale 7 (2015) 11093–11101.
[29] F. Lai, Y. Huang, Y. Miao, T. Liu, Controllable preparation of multi-dimensional hybrid materials of nickel-cobalt layered double hydroxide nanorods/nanosheets on electrospun carbon nanofibers for high-performance supercapacitors, Electrochim. Acta 174 (2015) 456–463.
[30] S. Zhang, Z. Huang, Z. Wen, L. Zhang, J. Jin, R. Shahbazian-Yassar, J. Yang, Local lattice distortion activate metastable metal sulfide as catalyst with stable full discharge-charge capability for Li-O_2 batteries, Nano Lett. 17 (2017) 3518–3526.
[31] L. Yang, Q. Fu, W. Wang, J. Huang, J. Huang, J. Zhang, B. Xiang, Large-area synthesis of monolayered $MoS_{2(1-x)}Se_{2x}$ with a tunable band gap and its enhanced electrochemical catalytic activity, Nanoscale 7 (2015) 10490–10497.
[32] J. Xu, X. Li, W. Liu, Y. Sun, Z. Ju, T. Yao, C. Wang, H. Ju, J. Zhu, S. Wei, Y. Xie, Carbon dioxide electroreduction into syngas boosted by a partially delocalized charge in molybdenum sulfide selenide alloy monolayers, Angew. Chem. Int. Ed. 56 (2017) 9121–9125.
[33] F. Lai, D. Yong, X. Ning, B. Pan, Y. Miao, T. Liu, Bionanofiber assisted decoration of few-layered $MoSe_2$ nanosheets on 3D conductive networks for efficient hydrogen evolution, Small 13 (2017), 1602866.
[34] S. Wang, B. Liu, G. Zhi, X. Gong, Z. Gao, J. Zhang, Relaxing volume stress and promoting active sites in vertically grown 2D layered mesoporous $MoS_{2(1-x)}Se_{2x}$/rGO composites with enhanced capability and stability for lithium ion batteries, Electrochim. Acta 268 (2018) 424–434.
[35] Y. Xu, L. Wang, X. Liu, S. Zhang, C. Liu, D. Yan, Y. Zeng, Y. Pei, Y. Liu, S. Luo, Monolayer MoS_2 with S vacancies from interlayer spacing expanded counterparts for highly efficient electrochemical hydrogen production, J. Mater. Chem. A 4 (2016) 16524–16530.
[36] H. He, D. Huang, Q. Gan, J. Hao, S. Liu, Z. Wu, W. Pang, B. Johannessen, Y. Tang, J. Luo, H. Wang, Z. Guo, Anion vacancies regulating endows MoSSe with fast and stable potassium ion storage, ACS Nano 13 (2019) 11843–11852.
[37] K. Xie, K. Yuan, X. Li, W. Lu, C. Shen, C. Liang, R. Vajtai, P. Ajayan, B. Wei, Superior potassium ion storage via vertical MoS_2 "nano-rose" with expanded interlayers on graphene, Small 13 (2017), 1701471.
[38] J. Ge, L. Fan, J. Wang, Q. Zhang, Z. Liu, E. Zhang, Q. Liu, X. Yu, B. Lu, $MoSe_2$/N-doped carbon as anodes for potassium-ion batteries, Adv. Energy Mater. 8 (2018), 1801477.
[39] X. Xiong, W. Luo, X. Hu, C. Chen, L. Qie, D. Hou, Y. Huang, Flexible membranes of MoS_2/C nanofibers by electrospinning as binder-free anodes for high-performance sodium-ion batteries, Sci. Rep. 5 (2015) 9254.
[40] S. Zhang, X. Yu, H. Yu, Y. Chen, P. Gao, C. Li, C. Zhu, Growth of ultrathin MoS_2 nanosheets with expanded spacing of (002) plane on carbon nanotubes for high-performance sodium-ion battery anodes, ACS Appl. Mater. Inter. 6 (2014) 21880–21885.
[41] D. Chao, P. Liang, Z. Chen, L. Bai, H. Shen, X. Liu, X. Xia, Y. Zhao, S. Savilov, J. Lin, Z. Shen, Pseudocapacitive Na-ion storage boosts high rate and areal capacity of self-branched 2D layered metal chalcogenide nanoarrays, ACS Nano 10 (2016) 10211–10219.
[42] V. Augustyn, J. Come, M. Lowe, J. Kim, P. Taberna, S. Tolbert, H. Abruña, P. Simon, B. Dunn, High-rate electrochemical energy storage through Li^+ intercalation pseudocapacitance, Nat. Mater. 12 (2013) 518–522.
[43] X. Xia, D. Chao, Y. Zhang, J. Zhan, Y. Zhong, X. Wang, Y. Wang, Z. Shen, J. Tu, H. Fan, Generic synthesis of carbon nanotube branches on metal oxide arrays exhibiting stable high-rate and long-cycle sodium-ion storage, Small 12 (2016) 3048–3058.
[44] D. Chao, C. Zhu, P. Yang, X. Xia, J. Liu, J. Wang, X. Fan, S. Savilov, J. Lin, H. Fan, Z. Shen, Array of nanosheets render ultrafast and high-capacity Na-ion storage by tunable pseudocapacitance, Nat. Commun. 7 (2016) 12122.